Progress toward development of low-temperature microwave refractive index gas thermometry at NRC

Rourke, P. M. C.; Hill, K. D.

Publisher's version / Version de l'éditeur:
https://doi.org/10.1007/s10765-014-1728-8
International Journal of Thermophysics, 36, 2, pp. 205-228, 2014-09-28

International Journal of Thermophysics manuscript No.
(will be inserted by the editor)

Progress toward development of low-temperature microwave refractive index gas thermometry at NRC

P. M. C. Rourke · K. D. Hill

Received: date / Accepted: date

Abstract Progress toward the development of a low-temperature microwave refractive index gas thermometry (RIGT) implementation for primary thermometry at NRC is reported. A prototype quasi-spherical copper resonator has been integrated into a cryogenic system with a 5 K base temperature, and preliminary microwave measurements in vacuum have been completed to characterize the resonator between 5 K and 297 K. The dependence of experimental results on spectral fitting background terms, first- and second-order shape corrections, and waveguide corrections has also been explored. The current NRC results agree with previous room-temperature measurements on the same resonator at NIST, and indicate no significant change in resonator shape between room temperature and low temperature. The temperature dependences of the resonator electrical conductivity and linear thermal expansion coefficient, as obtained from the microwave resonances, agree with published literature values for oxygen-free high-conductivity (OFHC) copper measured using other techniques.

Keywords Copper conductivity · Copper thermal expansion · Electromagnetic resonances · Microwaves · Quasi-spherical resonator · Refractive index gas thermometer

1 Introduction

1.1 $T - T_{90}$

Since its establishment, the International Temperature Scale of 1990 (ITS-90) [1,2] has formed the bedrock of worldwide temperature calibration activities. While the ITS-90 fixed point temperatures were assigned based on the best thermodynamic temperature data available at the time, recent experimental measurements of the differences between thermodynamic and ITS-90 temperatures ($T - T_{90}$) suggest significant deviations over a broad temperature range below the triple point of water.

National Research Council Canada, 1200 Montreal Road, Ottawa, ON K1A 0R6, Canada

Unfortunately, unexplained inconsistencies between data sets limit the usefulness of this data as a basis for a successor temperature scale to the ITS-90 [3]. These inconsistencies tend to occur between experimental techniques, principally between constant-volume gas thermometry (CVGT) data—upon which the ITS-90 is largely based—and newer acoustic gas thermometry (AGT) data [3]. There is also disagreement between dielectric-constant gas thermometry (DCGT), which finds that T_{90} is very close to T in the 2.5 K – 36 K range [4], and AGT, which shows significant deviations beginning at the neon point [5].

In order to resolve these inconsistencies, more experimental data is needed, particularly that collected using other methods of primary thermometry. One such technique that has not previously seen much use at low temperatures is refractive index gas thermometry (RIGT) [6–9], which leverages electromagnetic physics similar to DCGT in a large volume-to-surface-area form factor similar to AGT.

1.2 Refractive index gas thermometry (RIGT)

While early refractive index gas thermometry (RIGT) proposals were based on optical interferometry [6,7], microwave RIGT uses measurements of microwave resonances in a gas-filled conducting cavity at fixed temperature and gas pressure in order to determine the refractive index of the working gas. The thermodynamic temperature is then obtained from the refractive index via electromagnetic and density virial equations appropriate to the chosen working gas.

One approach for microwave RIGT implementation involves the use of quasi-spherical resonator (QSR) geometry, in which the microwave resonator is designed to deviate from a perfect sphere by small extensions ε_1 and ε_2 along two axes [8, 9]. This geometric deviation lifts the degeneracy of the $1m$ microwave modes in a controlled manner, splitting each spherical resonance into a triplet of peaks with centre frequencies f_i. Furthermore, the finite conductivity of the metal resonator allows some penetration of the microwaves into the resonator skin, causing each peak to be shifted and broadened by a half-width g_i. In practise, the frequencies and half-widths of each peak in a given triplet are measured, added together to correct for the penetration into the resonator skin, and then averaged across the triplet. The microwave refractive index n of the working gas is then determined by [8]

$$n(T,p) = \frac{c_0}{2\pi \langle f+g \rangle} \frac{\langle \xi_{\mathrm{corr}} \rangle}{a_{\mathrm{eq}}} \tag{1}$$

in which c_0 is the speed of light in vacuum, $\langle f+g \rangle$ is the average half-width-corrected frequency of the triplet, a_{eq} is the equivalent radius of a spherical resonator with the same volume as the measured QSR, and $\langle \xi_{\mathrm{corr}} \rangle$ is the average corrected microwave eigenvalue for the given mode. The corrected eigenvalues $\langle \xi_{\mathrm{corr}} \rangle$ differ from those of a perfect spherical resonator due to disturbances to the electromagnetic fields such as those caused by the quasi-spherical geometry [10] and the presence of waveguides (antennas and vent ports) [11]. Note also that there are two different mode types of interest, Transverse Magnetic (TM$1m$) and Transverse Electric (TE$1m$), each with their own set of eigenvalues.

To obtain the refractive index n from microwave resonance measurements via Eq. 1, it is important to have characterized both $\langle \xi_{corr} \rangle$ and a_{eq} for the particular resonator in use. In order to support the development of RIGT capabilities at NRC, in the present study we have characterized a quasi-spherical copper resonator by performing microwave measurements of the equivalent radius a_{eq}, the shape parameters ε_1 and ε_2, the electrical conductivity σ, and the linear thermal expansion coefficient α_L using numerous TM1m and TE1m modes in vacuum between 5 K and 297 K, and have compared the consistency of the results when applying different approaches for eigenvalue shape correction and waveguide correction.

2 Experimental details

2.1 Apparatus

The resonator used for the current study is an early prototype built at NIST using a design in which the deviation from sphericity comes from cylindrical "race-track" segments (see Fig. 1 of [8]). It is constructed from two oxygen-free high-conductivity (OFHC) copper hemispheres bolted together with stainless steel bolts at the equator, and has two vent ports to allow gas to communicate with the pressure vessel and two loop antennas to allow detection of both TM and TE modes. This resonator was previously characterized at room temperature at NIST [8], and is the microwave-only twin of the resonator previously used for a low-temperature AGT study [5].

As shown in Fig. 1, at NRC we have designed and built a copper pressure vessel to allow control of the resonator gas pressure. The resonator is hung from the lid of the pressure vessel using a threaded copper rod, into which has been machined a disc containing two thermometers (Rosemount CSPRT #4794 and Tinsley RhFe #A140) calibrated with respect to the ITS-90 fixed points. The calibrated thermometers are measured using Automatic Systems Laboratories F18 (#2847-002-158, for CSPRT #4794) and F900 (#7869-005-009, for RhFe #A140) primary thermometry bridges. CSPRT #4794 was used to realize T_{90} for temperatures greater than or equal to 13.8 K, while RhFe #A140 was used for temperatures less than 13.8 K. The pressure vessel is bolted onto the second stage of a two-stage Cryomech PT405 pulse tube cryocooler, surrounded by a radiation shield anchored to the first stage of the cryocooler and an additional room temperature vacuum jacket. Temperature control of the experiment is delivered by a combination of wrapped manganin and evanohm wire heaters and nickel-chromium cartridge heaters mounted on the cryocooler stage 1, stage 2 and the pressure vessel lid, orchestrated by a custom PID control algorithm. With all wiring and gas lines connected, this system is capable of stable temperature control down to 5 K. At the highest temperature measured, 297 K, data was collected with the cryocooler disengaged and the resonator temperature PID-stabilized against the natural cooling of the laboratory environment.

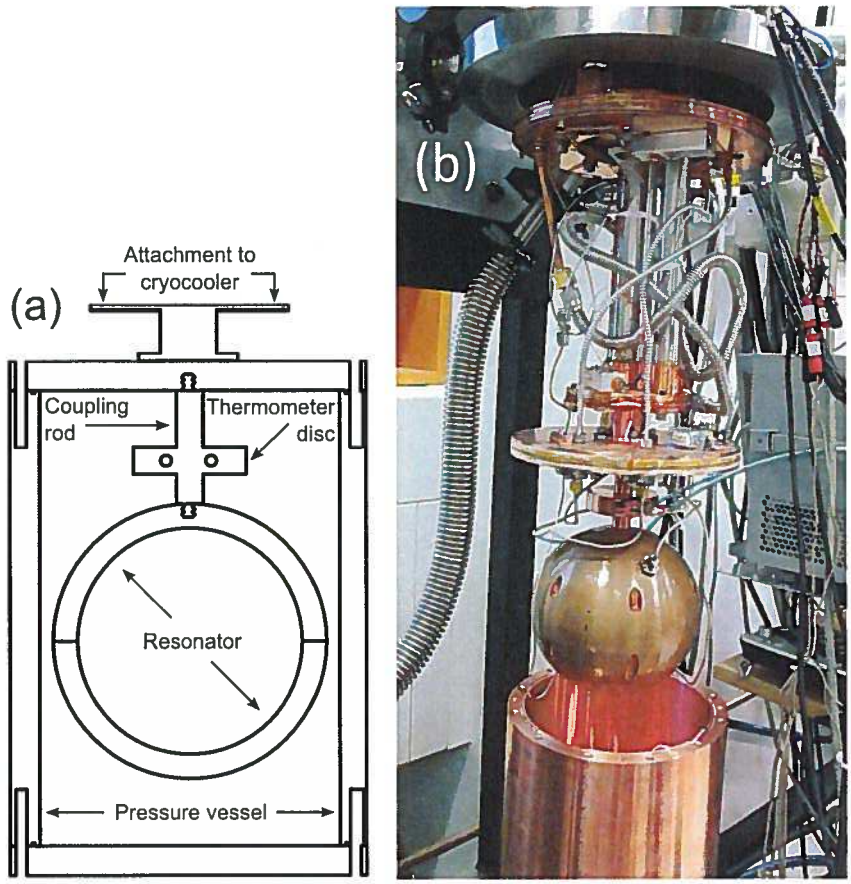

Fig. 1 Panel (a): resonator mount and pressure vessel design. Panel (b): photograph of apparatus, showing resonator, pressure vessel and cryocooler.

2.2 Microwave fitting

A 2-port Agilent N5230A PNA-L network analyzer is connected to the resonator antennas using short coaxial cables, and the microwave resonances for a given triplet are measured by recording the complex S_{21} parameter. The network analyzer data collection procedure has been optimized for best results across a variety of temperatures and microwave modes, including considerations of microwave heating of the resonator at low temperatures. For each microwave mode, the data collection software performs the following steps:

1. Predict the position of the triplet peaks
2. Perform a coarse -5 dB power, 5 Hz bandwidth network analyzer scan in which S_{21} data is collected at 301 equally-spaced frequencies in a large window encompassing all three predicted triplet peaks
3. Determine approximate positions of the actual peaks by running a peak detection routine on the coarse scan data

4. Perform fine −5 dB power, 5 Hz bandwidth network analyzer scans in which $\mathbf{S}_{21}$ data is collected at 101 equally-spaced frequencies in small windows centred on each of the three peaks in the triplet
5. Combine together the data from the coarse scan and three fine scans, and pre-analyze the composite scan to determine initial parameters for fitting
6. Fit the composite scan to extract the triplet peak frequencies and half-widths

The final fitting of the $\mathbf{S}_{21}$ composite scan data is performed using a complex Levenberg-Marquardt (LM) 3-Lorentzian + polynomial background fitting routine written by Eric May [8]. This algorithm determines the centre frequencies (f_1, f_2, f_3), half-widths (g_1, g_2, g_3) and associated fitting uncertainties $(\delta f_1, \delta f_2, \delta f_3, \delta g_1, \delta g_2, \delta g_3)$ of the peaks in the measured triplet, from which the average half-width-corrected frequency of the triplet $\langle f+g \rangle$ and its fitting uncertainty $\delta \langle f+g \rangle$ may be calculated.

The first 8 $1m$ microwave modes were measured in the present study: TM11, TE11, TM12, TE12, TM13, TE13, TM14 and TE14. In general, TM modes are found to have better signal-to-noise than TE modes and lower-frequency modes have better signal-to-noise than higher-frequency modes. The TM11 mode is the strongest and easiest to fit of all those measured—TM11 $\Re(\mathbf{S}_{21})$ and $\Im(\mathbf{S}_{21})$ data and fits collected in vacuum at 297 K and 5 K are shown in Fig. 2.

The TE14 mode is an example of one of the weaker and harder to fit modes measured—TE14 $\Re(\mathbf{S}_{21})$ and $\Im(\mathbf{S}_{21})$ data and fits collected in vacuum at 297 K and 5 K are shown in Fig. 3. Indeed, the small peak amplitudes of weaker modes like TE14 make their LM fits more susceptible to the influence of background effects and noise in the microwave spectrum.

2.3 Microwave background polynomial

In order to better reproduce the complicated microwave backgrounds seen in, e.g., Fig. 3, and reduce their influence on the fitted peak frequencies and half-widths, we explored the effects of varying background polynomial order on the fitted average triplet frequency $\langle f+g \rangle$ and its fitting uncertainty $\delta \langle f+g \rangle$ for all measured modes at 5 K and 297 K. As an example of an "easy-to-fit" mode, the results for TM11 are shown in Fig. 4: a 2nd- or 3rd-order polynomial allows stable $\langle f+g \rangle$ values and minimized $\delta \langle f+g \rangle$ values to be obtained, with little further change up to 9th order. As an example of a "hard-to-fit" mode, the results for TE14 are shown in Fig. 5: in this case, while the qualitative behaviour with increasing polynomial order is the same as for TM11, a higher polynomial order is required to obtain stable $\langle f+g \rangle$ values and minimized $\delta \langle f+g \rangle$ values; furthermore, the results diverge again at the highest orders tested as the fits begin to fail due to the presence of too many free parameters. By comparing similar background polynomial order tests for all measured modes, we find that a 7th-order polynomial is the overall best choice for "safe" fitting of all 8 modes at low and high temperatures, and therefore continue to use 7th-order polynomial backgrounds for all of the following analysis.

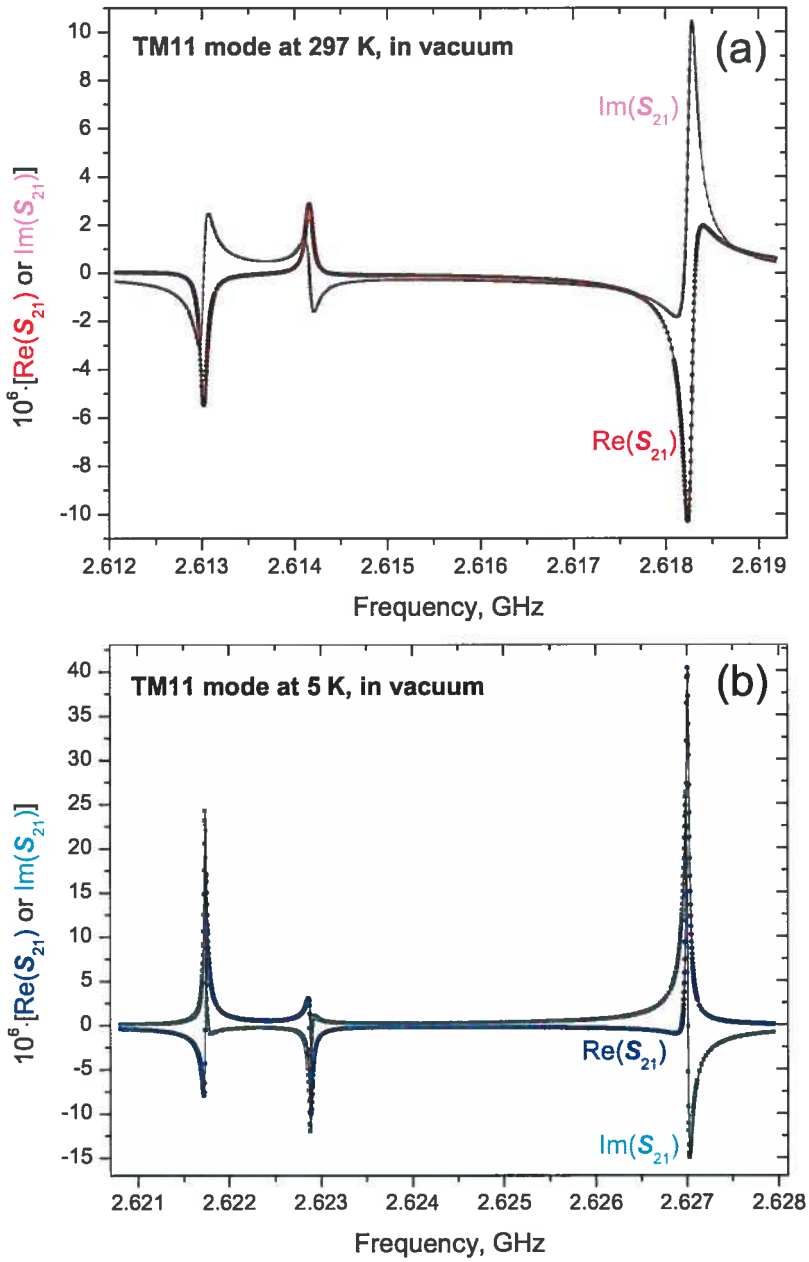

Fig. 2 Real and imaginary components of measured S_{21} parameter composite scans for the TM11 microwave mode, collected with the resonator under vacuum. Data in panel (a) was collected at 297 K; data in panel (b) was collected at 5 K. In both panels, the experimental data are shown as solid symbols: darker circles for the real component and lighter squares for the imaginary component. LM fits using 7th-order background polynomials are shown as black lines.

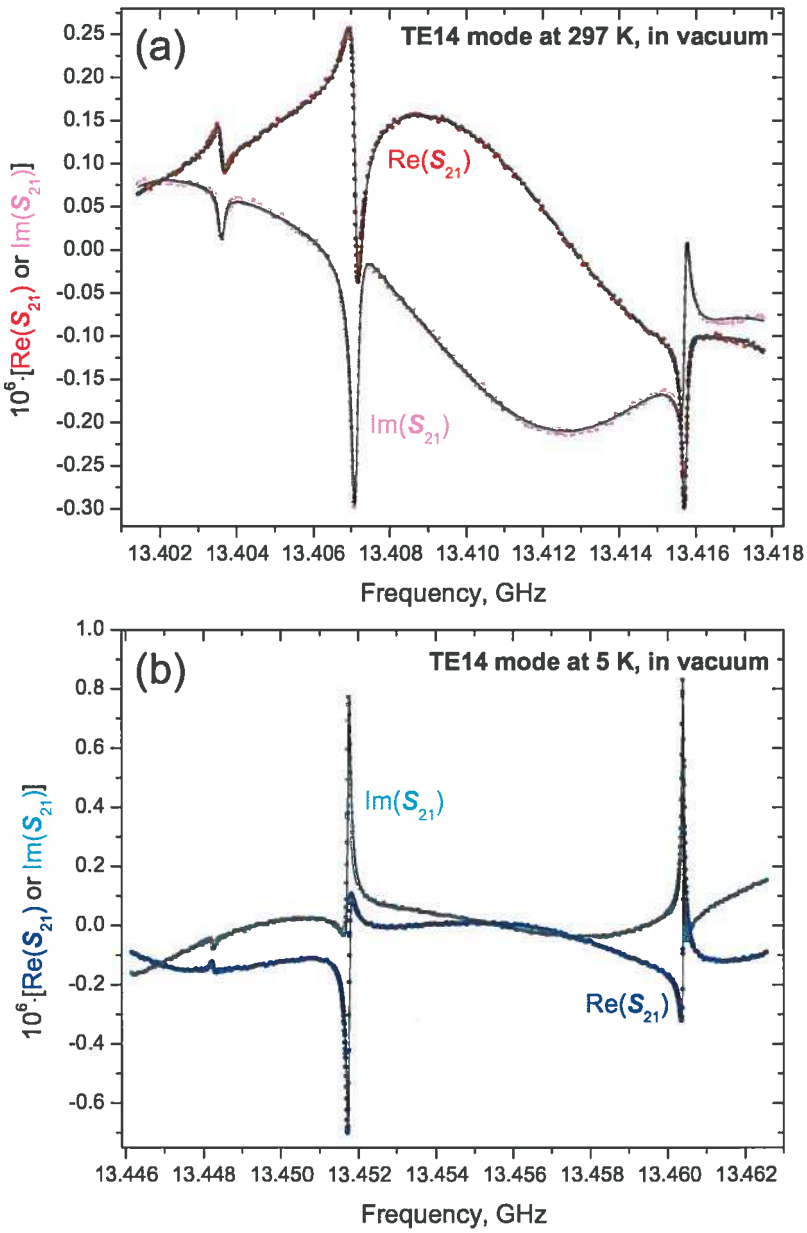

Fig. 3 Real and imaginary components of measured S_{21} parameter composite scans for the TE14 microwave mode, collected with the resonator under vacuum. Data in panel (a) was collected at 297 K; data in panel (b) was collected at 5 K. In both panels, the experimental data are shown as solid symbols: darker circles for the real component and lighter squares for the imaginary component. LM fits using 7th-order background polynomials are shown as black lines.

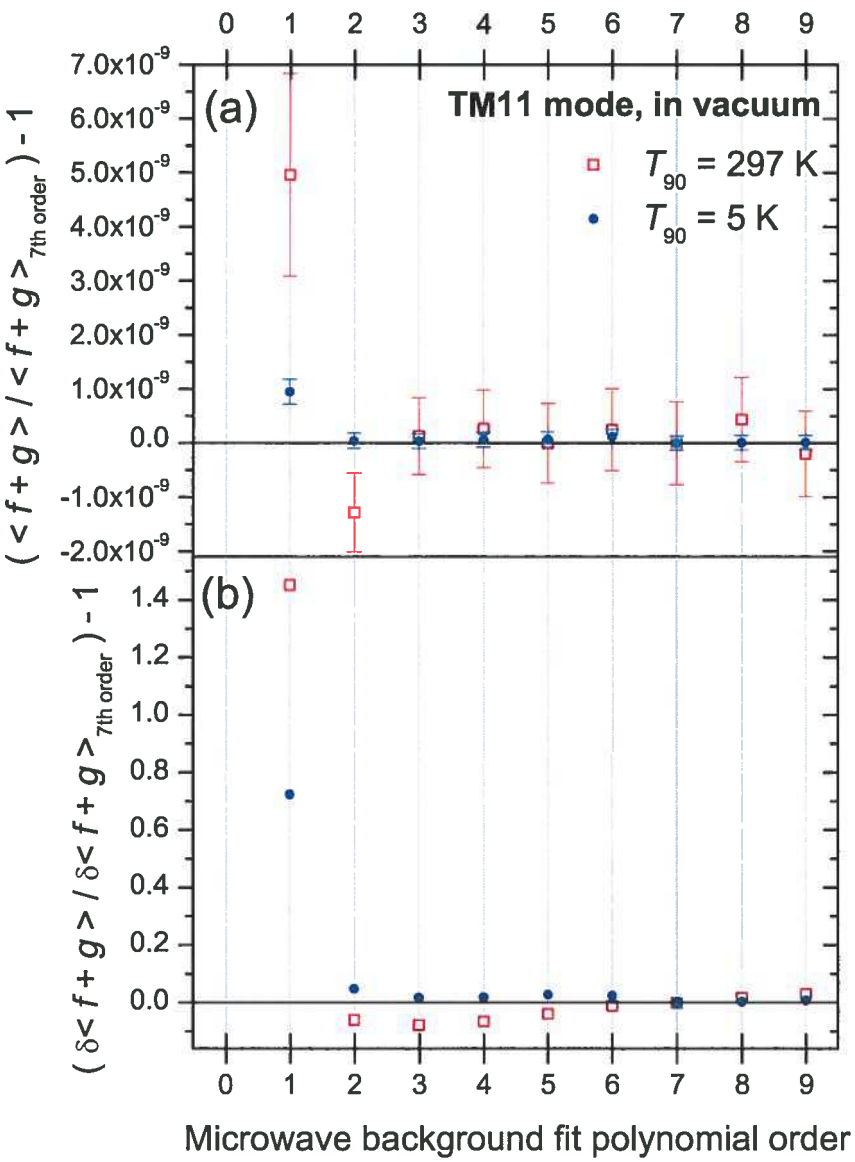

Fig. 4 LM fit results for fits to the TM11 experimental data shown in Fig. 2, using different polynomial background orders. For each fit, panel (a) shows the average half-width-corrected frequency of the triplet $\langle f+g\rangle$, and panel (b) shows its fitting uncertainty $\delta\langle f+g\rangle$. In both panels, 297 K results are shown as open squares, 5 K results are shown as solid circles, and the plotted values have been normalized to the 7th-order polynomial results from the fits shown as black lines in Fig. 2.

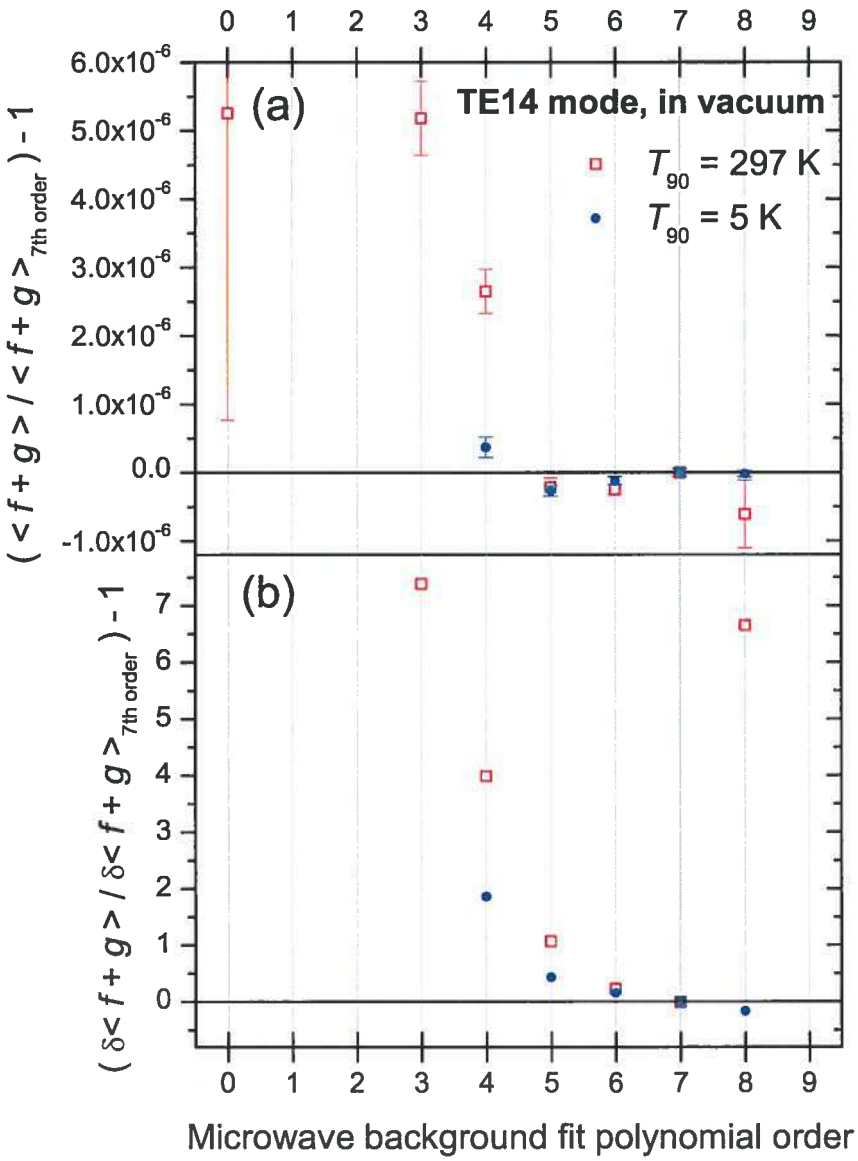

Fig. 5 LM fit results for fits to the TE14 experimental data shown in Fig. 3, using different polynomial background orders. For each fit, panel (a) shows the average half-width-corrected frequency of the triplet $\langle f+g \rangle$, and panel (b) shows its fitting uncertainty $\delta \langle f+g \rangle$. In both panels, 297 K results are shown as open squares, 5 K results are shown as solid circles, and the plotted values have been normalized to the 7th-order polynomial results from the fits shown as black lines in Fig. 3.

3 Corrections for waveguides and non-spherical shape

3.1 Waveguide correction

In order to account for the perturbative effects of waveguides on the microwave fields inside the resonator, we have implemented the corrections derived by Underwood *et al.* [11]. As a first step, we approximate the radius a' of the resonator by an estimate from Eq. 1 using the as-measured average half-width-corrected frequency of the triplet $\langle f+g \rangle$, the uncorrected spherical eigenvalue ξ in place of $\langle \xi_{\text{corr}} \rangle$, and an estimate of the refractive index n (note that $n \equiv 1$ for the vacuum measurements presented in the current study). Then the multiplicative correction Υ_i to the eigenvalue of peak i within the triplet is given by

$$\Upsilon_i = 1 + \sum_j X_{ij} \tag{2}$$

where j indexes the waveguides present in the resonator, and

$$\begin{aligned} X_{ij} = -\frac{r_{\text{h},j}^3}{\pi a'^3} \times \Bigg(\Bigg[\begin{Bmatrix} 0.339375, & \text{antenna} \\ 0.35625, & \text{vent port} \end{Bmatrix} \times \begin{Bmatrix} \frac{\xi^2}{\xi^2-2}, & \text{TM mode} \\ 1, & \text{TE mode} \end{Bmatrix} \times \\ \times \begin{Bmatrix} \cos^2\theta_j \sin^2\phi_j + \cos^2\phi_j, & i=1 \\ \cos^2\theta_j \cos^2\phi_j + \sin^2\phi_j, & i=2 \\ \sin^2\theta_j, & i=3 \end{Bmatrix} \Bigg] + \\ + \Bigg[\begin{Bmatrix} 0.546, & \text{coax antenna} \\ 0, & \text{loop antenna} \\ 0.864, & \text{vent port} \end{Bmatrix} \times \begin{Bmatrix} \frac{1}{\xi^2-2}, & \text{TM mode} \\ 0, & \text{TE mode} \end{Bmatrix} \times \\ \times \begin{Bmatrix} \sin^2\theta_j \sin^2\phi_j, & i=1 \\ \sin^2\theta_j \cos^2\phi_j, & i=2 \\ \cos^2\theta_j, & i=3 \end{Bmatrix} \Bigg] \Bigg) \end{aligned} \tag{3}$$

with $r_{\text{h},j}$ representing the given waveguide's radius and θ_j & ϕ_j specifying the waveguide's polar and azimuthal angular position in the resonator spherical coordinates—see Table 1 for the waveguide details of the resonator used in this study. The inclusion of a loop antenna case in Eq. 3 comes from a private communication of Robin Underwood to Laurent Pitre in [12], and is based on the idea that a loop will fill up more of the waveguide than a coaxial wire, therefore appearing somewhat like a solid wall to the electric field component of the microwaves but not to the magnetic field component.

For simplicity of data analysis code, rather than applying the above waveguide corrections directly to the resonator eigenvalues (leading to different eigenvalues for each peak in the triplet), we have instead opted to equivalently include the waveguide corrections at the level of the half-width-corrected frequencies of the peaks in the triplet, such that

$$(f_i + g_i)_{\text{wgcorr}} = (f_i + g_i)/\Upsilon_i \tag{4}$$

j	$r_{h,j}$ (mm)	θ_j (radians)	ϕ_j (radians)	waveguide type
1	1.55	$\pi/4$	$\pi/4$	loop antenna
2	1.55	$3\pi/4$	$3\pi/4$	loop antenna
3	0.8	$\pi/4$	$5\pi/4$	vent port
4	0.415	0	0	vent port

Table 1 Summary of radii, angular positions and types of waveguides in the resonator used in this study.

3.2 Shape correction

Following the work of Mehl in [10], by comparing the relative frequencies of the peaks within each triplet we determine the values of the parameters ε_1 and ε_2 that characterize the deviation of the resonator shape from a perfect sphere. Specifically, ε_1 and ε_2 are obtained by solving the coupled equations

$$\left[\frac{(f_2+g_2)_{\text{wgcorr}}}{(f_1+g_1)_{\text{wgcorr}}}\right]^2 = \frac{A_{1,y}\varepsilon_1 + A_{2,x}\varepsilon_2 + B_{11,y}\varepsilon_1^2 + B_{12,x}\varepsilon_1\varepsilon_2 + B_{22,x}\varepsilon_2^2 + 1}{A_{1,y}\varepsilon_1 + A_{1,y}\varepsilon_2 + B_{11,y}\varepsilon_1^2 + B_{12,y}\varepsilon_1\varepsilon_2 + B_{11,y}\varepsilon_2^2 + 1} \tag{5}$$

$$\left[\frac{(f_3+g_3)_{\text{wgcorr}}}{(f_1+g_1)_{\text{wgcorr}}}\right]^2 = \frac{A_{2,x}\varepsilon_1 + A_{1,y}\varepsilon_2 + B_{22,x}\varepsilon_1^2 + B_{12,x}\varepsilon_1\varepsilon_2 + B_{11,y}\varepsilon_2^2 + 1}{A_{1,y}\varepsilon_1 + A_{1,y}\varepsilon_2 + B_{11,y}\varepsilon_1^2 + B_{12,y}\varepsilon_1\varepsilon_2 + B_{11,y}\varepsilon_2^2 + 1} \tag{6}$$

where, for TM modes, the A and B parameters are calculated from the unperturbed spherical eigenvalue ξ by

$$A_{1,y,\text{TM}} = -\frac{(\xi^2+4)}{8(\xi^2-2)} \tag{7}$$

$$A_{2,x,\text{TM}} = \frac{(\xi^2+4)}{4(\xi^2-2)} \tag{8}$$

$$B_{\ell,\zeta,\text{TM}} = \begin{cases} 0, & \text{1st-order shape correction} \\ \displaystyle\sum_{k=0}^{4} \frac{C_{k,\ell,\zeta,\text{TM}}\xi^k}{7875\xi^3}, & \text{2nd-order shape correction} \end{cases} \tag{9}$$

and, for TE modes,

$$A_{1,y,\text{TE}} = -\frac{1}{8} \tag{10}$$

$$A_{2,x,\text{TE}} = \frac{1}{4} \tag{11}$$

$$B_{\ell,\zeta,\text{TE}} = \begin{cases} 0, & \text{1st-order shape correction} \\ \displaystyle\sum_{k=0}^{1} \frac{C_{k,\ell,\zeta,\text{TE}}\xi^k}{7875}, & \text{2nd-order shape correction} \end{cases} \tag{12}$$

The coefficients $C_{k,\ell,\zeta}$ in Eqs. 9 and 12, derived from [10] after a typographical error in the numerator of Eq. 13 of [10] is corrected from 8420 to 8240, are listed in Table 2. Note that while the A parameters in Eqs. 7, 8, 10 and 11 are written specifically for the "race-track" geometry (and therefore differ from Eqs. 5–8 in [10]), the

$B_{\ell,\zeta}$	$B_{11,y}$	$B_{12,y}$	$B_{12,x}$	$B_{22,x}$
$C_{0,\ell,\zeta,\mathrm{TM}}$	11920	−7360	320	−17120
$C_{1,\ell,\zeta,\mathrm{TM}}$	−21924	14112	17136	−4536
$C_{2,\ell,\zeta,\mathrm{TM}}$	12318	−19284	−5352	5352
$C_{3,\ell,\zeta,\mathrm{TM}}$	−4040	7970	1160	−2210
$C_{4,\ell,\zeta,\mathrm{TM}}$	621	−1098	−144	144
$C_{0,\ell,\zeta,\mathrm{TE}}$	640	−670	440	−1490
$C_{1,\ell,\zeta,\mathrm{TE}}$	621	−1098	−144	144

Table 2 Numerical values of the coefficients $C_{k,\ell,\zeta}$ in Eqs. 9 and 12.

B parameters and C coefficients in Eqs. 9, 12 and Table 2 were derived for a different "triaxial ellipsoid" geometry. Unfortunately, no derivation of the 2nd-order eigenvalue shape correction yet exists for the "race-track" geometry, so even though we have a "race-track" resonator, in the present study we have used the B parameters and C coefficients derived for the "triaxial ellipsoid" geometry.

Once the shape parameters ε_1 and ε_2 have been obtained, the shape-corrected eigenvalue $\xi_{\mathrm{corr},i}$ of each peak i in the triplet is calculated as [10]

$$\xi_{\mathrm{corr},i} = \xi \times \begin{cases} \sqrt{A_{1,y}\varepsilon_1 + A_{1,y}\varepsilon_2 + B_{11,y}\varepsilon_1^2 + B_{12,y}\varepsilon_1\varepsilon_2 + B_{11,y}\varepsilon_2^2 + 1}, & i = 1 \\ \sqrt{A_{1,y}\varepsilon_1 + A_{2,x}\varepsilon_2 + B_{11,y}\varepsilon_1^2 + B_{12,x}\varepsilon_1\varepsilon_2 + B_{22,x}\varepsilon_2^2 + 1}, & i = 2 \\ \sqrt{A_{2,x}\varepsilon_1 + A_{1,y}\varepsilon_2 + B_{22,x}\varepsilon_1^2 + B_{12,x}\varepsilon_1\varepsilon_2 + B_{11,y}\varepsilon_2^2 + 1}, & i = 3 \end{cases} \quad (13)$$

with the average shape-corrected eigenvalue $\langle \xi_{\mathrm{corr}} \rangle$ following as

$$\langle \xi_{\mathrm{corr}} \rangle = (\xi_{\mathrm{corr},1} + \xi_{\mathrm{corr},2} + \xi_{\mathrm{corr},3})/3 \quad (14)$$

4 Resonator characterization results

A preliminary set of microwave measurements were obtained from several TM and TE modes, with the resonator in vacuum at temperatures ranging from 5 K to 297 K. As described in Section 2.3, all microwave spectra were fitted using a 7th-order polynomial background. The resonator shape parameters ε_1 and ε_2 were determined using the approach described in Section 3.2, and since the refractive index $n \equiv 1$ in vacuum, Eq. 1 was used to obtain the equivalent spherical radius of the resonator a_{eq} from the microwave data.

4.1 Microwave mode dependence

In order to compare the consistency of the experimental results across the various microwave modes measured, and to explore the effects of corrections and temperature changes on this mode-to-mode consistency, the measured a_{eq}, ε_1 and ε_2 values are plotted in Figs. 6–8 versus the average half-width-corrected frequency of each mode.

4.1.1 Comparison to previous measurements

The previous measurements performed on this resonator at 290 K by May *et al.* at NIST [8] are shown as asterisk symbols in Fig. 6. May *et al.* measured the first 4 microwave modes and analyzed their data using a 1st-order shape correction but no waveguide corrections; their results show clear trends with increasing mode frequency. For comparison, the experimental results from the present study, taken at 297 K and analyzed with a similar 1st-order shape / no waveguide correction approach, are plotted as open diamonds in Fig. 6.

The a_{eq} values obtained in the present study are offset from those of May *et al.* due to thermal expansion of the resonator between 290 K and 297 K; and since ε_1 parametrizes the extension of the resonator along the axis perpendicular to the equatorial plane, we believe the offset between ε_1 values indicates that the two resonator hemispheres were bolted together more tightly at NRC than they were at NIST. However, beyond these offsets, the consistent mode-to-mode dependences of a_{eq}, ε_1 and ε_2 found in the measurements of May *et al.* and those of the present study, performed almost 10 years later with different experimental apparatus at a different NMI, serve to increase confidence in the NRC RIGT set-up and show that the resonator geometry has been maintained between both experiments.

4.1.2 Shape correction

The experimental results obtained in the present study were also analyzed with the correction due to non-spherical resonator shape taken to 2nd order, as described in Section 3.2. These are plotted as open circles in Fig. 6, starting from the same 297 K data set as the 1st-order-corrected open diamonds in that figure, without any waveguide correction. It is immediately apparent that going from a 1st-order shape correction to a 2nd-order shape correction dramatically changes the mode-to-mode dependence of the results: this tells us that the details of the shape correction are important to the analysis of the microwave resonances. Furthermore, the results obtained using a 2nd-order shape correction have better mode-to-mode consistency than those obtained using a 1st-order-only correction, which indicates that the 2nd-order approach better captures the physics of the real resonator than does the 1st-order approach.

However, the 2nd-order-shape-corrected results still show some residual trends with increasing mode frequency, indicating that there is room to improve the shape correction approach of Section 3.2. This is not surprising, because: 1) the 2nd-order shape correction described in Section 3.2 was derived for a "triaxial ellipsoid" geometry, not the "race-track" geometry of the present resonator design; and 2) coordinate measurement machine (CMM) dimensional measurements of this resonator reported by May *et al.* revealed that the as-manufactured resonator cavity deviated somewhat from the "race-track" design [8]. Future improvements to the treatment of shape correction for this resonator could include deriving a 2nd-order correction specific to the "race-track" case, or implementing an approach based on modal superposition [13].

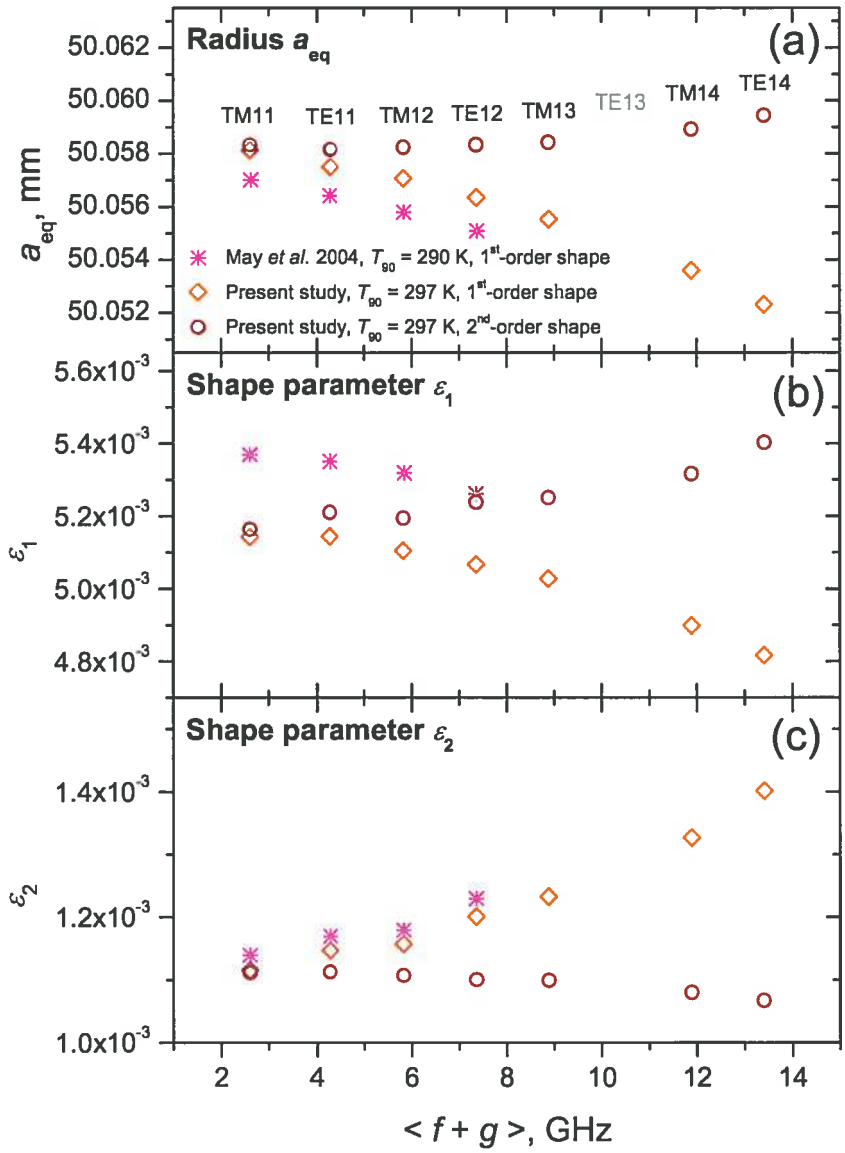

Fig. 6 Microwave resonator characterization of equivalent radius a_{eq} (panel (a)), shape parameter ε_1 (panel (b)), and shape parameter ε_2 (panel (c)) measured in vacuum near room temperature, plotted versus the average half-width-corrected frequency of each microwave mode. Asterisk symbols represent measurements done at NIST at 290 K, using a 1st-order shape correction, by May *et al.* [8]. Open diamonds represent measurements done at NRC at 297 K in the present study, analyzed using a 1st-order shape correction. Open circles show the same 297 K NRC measurements as the open diamonds, but analyzed using a 2nd-order shape correction. No waveguide corrections were applied to any of the plotted data sets. In all cases, error bars propagated from the microwave fitting uncertainties are smaller than the data symbols. In the present study, 297 K results were not obtained for the TE13 mode due to one peak in the triplet falling below the noise floor at this temperature.

4.1.3 Waveguide correction

The effects of including waveguide corrections (Section 3.1), in addition to the 2nd-order shape correction, are shown in Fig. 7. As expected from the form of Eq. 3, the waveguide corrections are largely independent of microwave mode type, microwave mode frequency, and resonator temperature (not shown); they have a minimal effect on the obtained values of ε_1 and ε_2, and do not change the mode-to-mode trends of any of a_{eq}, ε_1 or ε_2.

Since the waveguide correction approach for loop antennas discussed in Section 3.1 is more speculative than that derived for straight coaxial antennas, we have compared its effect on our results (open squares in Fig. 7) to a case in which the antennas are treated as coaxial antennas ($\times$ symbols in Fig. 7). In the context of our experimental data, the two different waveguide correction approaches are found to be almost identical, except for a small change in the TM11 value of a_{eq}. Since there is little difference between the coax and loop results, we have elected to keep the loop antenna correction (corresponding to the actual loop antennas in our resonator) for the further analysis presented below.

4.1.4 Temperature dependence

Fig. 8 shows experimental results analyzed with a 2nd-order shape correction and a loop-antenna-based waveguide correction, collected at 297 K (open squares) and 5 K (solid circles). The resonator contracts significantly during cooling, so in order to compare the mode-to-mode dependence of a_{eq} at high and low temperatures, the plotted 5 K a_{eq} values have been multiplied by a single numerical factor in order to scale the 5 K TM11 a_{eq} up to the 297 K TM11 a_{eq} value. No scaling has been applied to the ε_1 and ε_2 values.

The data plotted in Fig. 8 reveal that the resonator's shape is remarkably consistent at high and low temperatures: as evidenced by both the 297 K – 5 K agreement of shape parameters ε_1 and ε_2, and the similar mode-to-mode trends of a_{eq}, ε_1 and ε_2 arising from the same uncorrected residual shape perturbations at both temperatures. Although the resonator's size changes considerably over this temperature range, the fact that its shape stays the same raises the possibility that future RIGT experiments could be performed by ratiometrically comparing measurements of the same microwave mode at different temperatures, thereby cancelling out the residual uncorrected shape perturbation.

4.2 Copper electrical conductivity

Since the finite electrical conductivity of the metal resonator allows the microwaves to penetrate into a thin layer of the resonator cavity and therefore broadens the resonance peaks, it is possible to work backwards from measurements of the microwave peak half-widths to obtain the conductivity of the copper in this thin "skin" layer. Specifically, the product of the relative magnetic permeability $\mu_{r,Cu}$ and the electrical

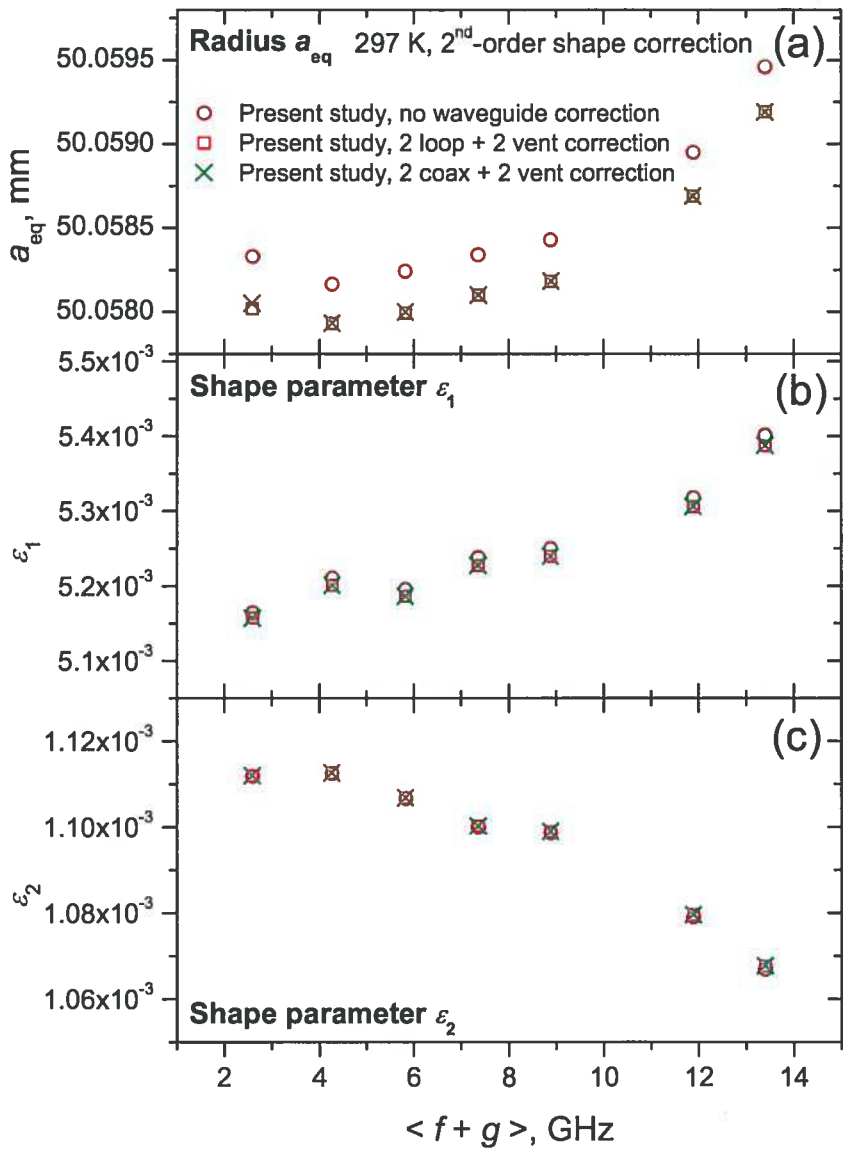

Fig. 7 Microwave resonator characterization of equivalent radius a_{eq} (panel (a)), shape parameter ε_1 (panel (b)), and shape parameter ε_2 (panel (c)) measured in vacuum at 297 K, plotted versus the average half-width-corrected frequency of each microwave mode. All plotted data sets were analyzed using a 2nd-order shape correction. Open circles here are the same as the open circles in Fig. 6, and do not include any waveguide corrections. Open squares show the same measurements as the open circles, but with a waveguide correction corresponding to the 2 loop antennas and 2 vent ports listed in Table 1. × symbols are the same as the open squares, but with the antennas treated as straight coaxial antennas instead of loop antennas. In all cases, error bars propagated from the microwave fitting uncertainties are smaller than the data symbols.

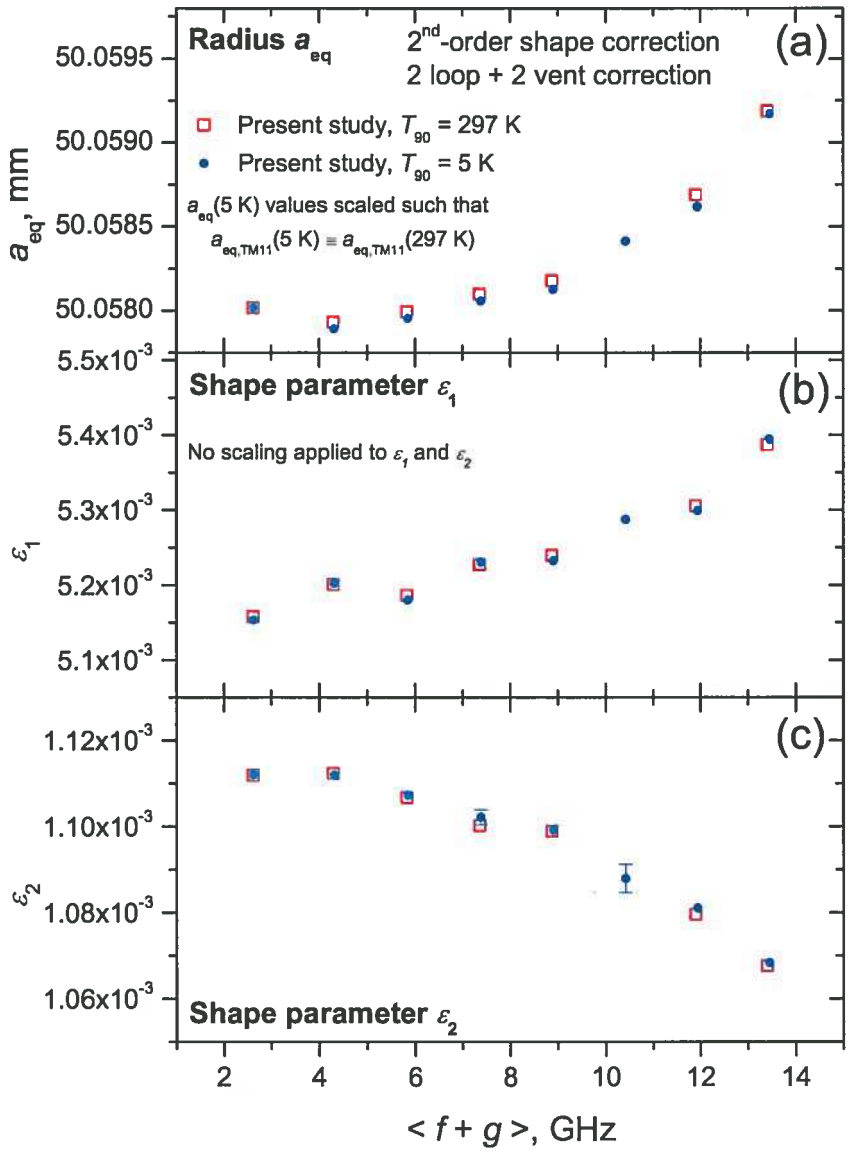

Fig. 8 Microwave resonator characterization of equivalent radius a_{eq} (panel (a)), shape parameter ε_1 (panel (b)), and shape parameter ε_2 (panel (c)) measured in vacuum at room temperature and low temperature, plotted versus the average half-width-corrected frequency of each microwave mode. Open squares represent measurements done at 297 K (same as open squares in Fig. 7), whereas solid circles represent those done at 5 K. Both data sets include a waveguide correction corresponding to the waveguides listed in Table 1 and a 2nd-order shape correction. For ease of comparison, in panel (a) the 5 K a_{eq} values have been multiplied by a single numerical factor in order to fix the 5 K TM11 a_{eq} to its value at 297 K; no scaling has been applied to ε_1 or ε_2. Except where shown, error bars propagated from the microwave fitting uncertainties are smaller than the data symbols.

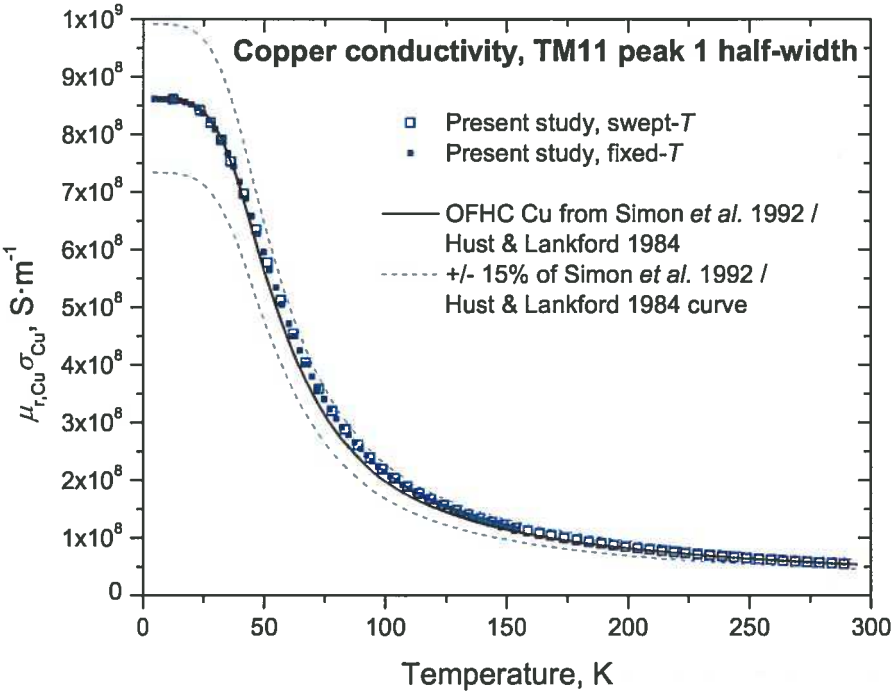

Fig. 9 Electrical conductivity of the resonator skin layer, as obtained from the TM11 peak 1 half-width measured in vacuum under swept-temperature (open squares) and fixed-temperature (solid squares) conditions in the present study. Literature values for OFHC copper from Eqs. 16–19 [14, 15] are plotted as a solid black line, with the free parameter ρ_0 determined from the present study fixed-temperature data at 5 K. ±15% bounds on the literature curve [14] are plotted as dashed grey lines.

conductivity σ_{Cu} may be calculated from a given peak i in a microwave triplet using the equation [8]

$$(\mu_{r,Cu}\sigma_{Cu})_i = \frac{(f_i + g_i)_{wgcorr}}{4\pi\mu_0 g_i^2} \times \begin{cases} \left[\dfrac{\xi^2_{corr,i}}{\xi^2_{corr,i} - 2}\right]^2, & \text{TM mode} \\ 1, & \text{TE mode} \end{cases} \tag{15}$$

in which $\mu_0 = 4\pi \times 10^{-7}$ V·s·A^{-1}·m^{-1} is the magnetic constant, g_i is the half-width of peak i, $(f_i + g_i)_{wgcorr}$ is the waveguide-corrected, half-width-corrected centre frequency of peak i, and $\xi_{corr,i}$ is the shape-corrected eigenvalue of peak i. This approach includes both the waveguide correction and the 2nd-order shape correction.

Certain microwave resonance peaks—peak 3 for TM modes and peaks 1 and 2 for TE modes—have surface currents that cross the equatorial joint between the two resonator hemispheres, resulting in additional broadening of these peaks. To avoid this effect, while still using the strongest and easiest-to-fit microwave mode, we have calculated $\mu_{r,Cu}\sigma_{Cu}$ from our measurements of peak 1 of the TM11 mode; these experimental results are plotted versus resonator temperature in Fig. 9.

As a first approach, plotted as open squares in Fig. 9, microwave scans were performed periodically as the temperature of the resonator was slowly and continuously swept from 5 K to 297 K. The temperature sweep rate gradually reduced as the thermal response of the system slowed with rising temperature, but the temperature sweep was not interrupted when microwave scans were performed, leading to non-constant temperatures within each scan. More refined measurements, plotted as solid squares in Fig. 9, were then done by stabilizing the resonator at each measurement temperature prior to each microwave scan.

In order to compare the temperature dependence of our measured resonator conductivity to typical literature data for oxygen-free high-conductivity (OFHC) copper, we have referred to the work of Simon *et al.* [14]. In their monograph, Simon *et al.* have compiled, reviewed and analyzed a large number of previous studies of a wide variety of mechanical and physical properties of copper and copper alloys at cryogenic temperatures [14]. For the electrical resistivity ρ of copper, Simon *et al.* refer to previous collation and analysis by Hust and Lankford [15]. They found that the temperature dependence of the collection of previous literature measurements on OFHC copper from 2 K to 900 K could be reproduced to within $\pm 15\%$ by the following equations [14, 15]

$$\sigma_{Cu}\left[\mathrm{S}\cdot\mathrm{m}^{-1}\right] = \left\{\rho\left[\Omega\cdot\mathrm{m}\right]\right\}^{-1} = \left[\rho_0 + \rho_i + \rho_{i0}\right]^{-1} \tag{16}$$

$$\rho_i\left[\Omega\cdot\mathrm{m}\right] = \frac{\left(1.171\times10^{-17}\right)T_{90}^{4.49}}{1+\left(1.171\times10^{-17}\right)\left(3.841\times10^{10}\right)T_{90}^{4.49-1.14}\exp\left[-\left(50/T_{90}\right)^{6.428}\right]} \tag{17}$$

$$\rho_{i0}\left[\Omega\cdot\mathrm{m}\right] = \frac{0.4531\rho_i\rho_0}{\left(\rho_i+\rho_0\right)} \tag{18}$$

Note that in Eqs. 16–18 a typographical error in the units of [14] has been corrected from $\mathrm{n}\Omega\cdot\mathrm{m}$ to $\Omega\cdot\mathrm{m}$, and in Eq. 17 a typographical error in an exponent of [14, 15] has been corrected from $+1.14$ to -1.14.

Simon *et al.* also find that the literature measurements of the magnetic susceptibility of OFHC copper lead to a relative magnetic permeability that can be represented in the 1.4 K – 300 K range by [14]

$$\mu_{r,Cu} = 1 + \left[\left(3.59/T_{90}\right) - 9.84 + \left(6.66\times10^{-4}T_{90}\right)\right]\times10^{-6} \tag{19}$$

Although $\mu_{r,Cu}$ stays within 10 parts per million of 1 over the entire temperature range of interest, and therefore has little influence relative to the $\pm 15\%$ bounds on σ_{Cu}, we have included it in our comparison for completeness.

The literature temperature dependence of $\mu_{r,Cu}\sigma_{Cu}$ for OFHC copper from Eqs. 16–19 [14, 15] is plotted as a solid black line in Fig. 9; the $\pm 15\%$ bounds on the literature curve are plotted as dashed grey lines. The residual resistivity ρ_0 is a free parameter in Eqs. 16 and 18, so it has been fixed based on the 5 K fixed-temperature experimental value of $\mu_{r,Cu}\sigma_{Cu}$ from TM11 peak 1 in the present study.

The agreement between our experimental data and the temperature dependence of the literature curve shown in Fig. 9 is encouraging, particularly since the present study used a very different experimental technique (microwave resonance measurements

in the gigahertz range) than did the studies collected in the literature (4-point DC resistivity measurements), and no corrections were included for effects such as cold-working of the resonator surface, a dielectric layer deposited on the resonator surface, or the low-temperature anomalous skin effect [16].

4.3 Copper thermal expansion coefficient

The microwave measurements from the present study's swept-temperature and fixed-temperature data sets (described in Section 4.2) can also be used to calculate the thermal expansion of the resonator. Each data set contains a series of a_{eq} values for each microwave mode, measured sequentially at temperatures rising from 5 K to 297 K, obtained from microwave scan data in vacuum using Eq. 1. The linear thermal expansion coefficient α_L of the resonator at microwave scan p, determined relative to microwave scan q, is given by

$$\alpha_L(T_{90,p})\big|_q = \frac{a_{eq,p} - a_{eq,q}}{a_{eq,q} \times (T_{90,p} - T_{90,q})} \tag{20}$$

where $T_{90,p}$ and $T_{90,q}$ are the average temperatures measured by the relevant ITS-90-calibrated thermometer during scans p and q, respectively. The waveguide and 2nd-order shape corrections from Section 3 are included in the a_{eq} values, but since $\alpha_L(T_{90,p})\big|_q$ is calculated ratiometrically, these corrections should drop out of the obtained thermal expansion coefficient data. We calculate the final α_L value at microwave scan p as the average of the $\alpha_L(T_{90,p})\big|_q$ values determined relative to the next nearest microwave scans on the lower- and higher-temperature sides of scan p ("$p-1$" and "$p+1$", respectively) in the data series

$$\alpha_L(T_{90,p}) = \frac{1}{2}\left[\alpha_L(T_{90,p})\big|_{q=p-1} + \alpha_L(T_{90,p})\big|_{q=p+1}\right] \tag{21}$$

The experimentally-measured values of α_L for the resonator used in this study, calculated from a_{eq} via Eqs. 20 and 21, are plotted in Fig. 10(a). Results obtained from the first three microwave modes are shown: TM11 as squares, TE11 as circles and TM12 as diamonds; with open symbols representing data from the swept-temperature data set and solid symbols representing data from the fixed-temperature data set. Results obtained from higher-frequency, harder-to-fit microwave modes (not shown) are consistent with those from the first three modes, but with more scatter and larger fitting uncertainties.

The linear thermal expansion coefficient of copper is another physical property for which Simon *et al.* have compiled, reviewed and analyzed literature data [14]. They performed regression analysis and found that the best fit to the collection of OFHC copper literature α_L values from 4 K to 300 K was obtained with the equation [14]

$$\log_{10}\alpha_{L,\text{literature}}(T_{90}) = \sum_{k=0}^{6} C_{\alpha_L,k}(\log_{10}T_{90})^k \tag{22}$$

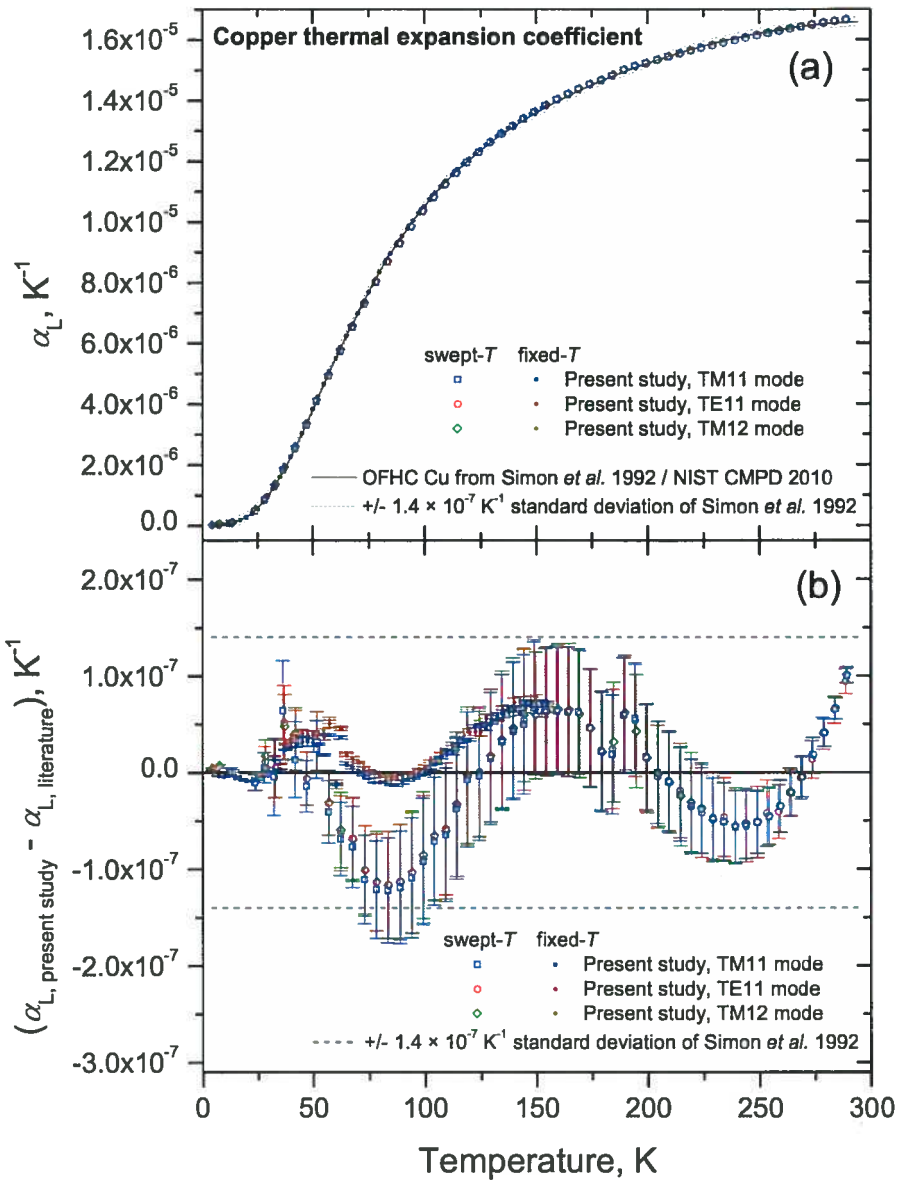

Fig. 10 Panel (a): discrete symbols show the linear coefficient of thermal expansion α_L experimentally determined for the current copper resonator using microwave resonance measurements of a_{eq} and Eqs. 20 and 21. Data from the TM11 mode are shown as squares, from the TE11 mode as circles and from the TM12 mode as diamonds; with open symbols representing data from the swept-temperature data set and solid symbols representing data from the fixed-temperature data set. The literature curve for OFHC copper, from Eq. 22 [14] and Table 3 [17], and its one-standard-deviation bounds [14] are shown as a solid black line and dashed grey lines, respectively. Panel (b): the same data as panel (a), but with the literature curve subtracted. Error bars for the present study data are propagated from the microwave fitting uncertainty and temperature standard deviation within each microwave scan.

k	$C_{\alpha_L,k}$
0	−17.9081289
1	67.131914
2	−118.809316
3	109.9845997
4	−53.8696089
5	13.30247491
6	−1.30843441

Table 3 Numerical values of the coefficients $C_{\alpha_L,k}$ in Eq. 22 from the NIST Cryogenic Materials Properties Database, 2010 revision [17].

in which $\alpha_{L,\text{literature}}$ has units of 10^{-6} K^{-1}. The linear standard deviation of Simon *et al.*'s fit to the literature data is 0.14×10^{-6} K^{-1}. Unfortunately, the values of the fit coefficients $C_{\alpha_L,k}$ listed in [14] are incorrect and do not match Simon *et al.*'s actual fit to the literature data (as shown correctly in their figures and data tables). The correct $C_{\alpha_L,k}$ values corresponding to the original literature fit of Simon *et al.* have been posted to NIST's online Cryogenic Materials Properties Database (CMPD) [17] and are listed in Table 3. Note that only the CMPD 2010 revision has the correct $C_{\alpha_L,k}$ values; the pre-2010 version of the CMPD website showed a different, incorrect set of $C_{\alpha_L,k}$ coefficients.

The literature curve for OFHC copper $\alpha_{L,\text{literature}}$ from Eq. 22 and Table 3 is plotted in Fig. 10(a) as a solid black line, with the bounds from the 0.14×10^{-6} K^{-1} literature standard deviation [14] shown as dashed grey lines. In Fig. 10(b), the experimental α_L data from the present study is shown with the literature curve subtracted.

The agreement between the present microwave measurements of the thermal expansion of the resonator and the literature values for the thermal expansion of OFHC copper is excellent. While the unstable resonator temperature during the scans of the initial data set collected with continuously-swept temperature exaggerates the deviations from the literature values, both that data set and the improved data set measured at fixed temperatures are within the 0.14×10^{-6} K^{-1} standard deviation of the literature curve over the entire measured temperature range. This agreement is especially striking since there are no free parameters in the literature curve—it is entirely independent of the measurements made in the present study—and the present measurements were performed on a composite object with a very different experimental technique than the previous thermal expansion measurements found in the literature.

5 Summary

We have performed microwave resonance measurements to characterize a copper quasi-spherical "race-track" resonator in vacuum between 5 K and 297 K. We measured the first eight microwave modes and find that the complicated microwave backgrounds require 7th-order background polynomials in order to obtain the optimum fit results for the microwave triplets at low and high temperatures.

The mode-to-mode dependences of our measured equivalent radius a_{eq} and shape parameters ε_1 and ε_2 agree with those measured previously for the same resonator at

NIST [8]. Including a 2nd-order correction for the resonator's non-spherical shape [10] increases the consistency between results obtained from different microwave modes, but there is room to improve this correction in the future by tailoring it more specifically to the geometry of the resonator. The perturbing effects of waveguides connecting to the resonator cavity [11] are largely independent of microwave mode type, microwave mode frequency, resonator temperature, and antenna type, and the resonator shape is preserved even as the resonator size changes between high and low temperature. This raises the possibility that shape and waveguide corrections may be cancelled out of future experimental results by performing ratiometric measurements of the same modes at different temperatures.

The temperature dependences of the electrical conductivity and linear thermal expansion coefficient of the resonator, calculated from the microwave resonance measurements, show excellent agreement with literature values of these properties for OFHC copper [14,15,17]. The strong agreement with literature values measured by entirely different experimental techniques validates our implementation of the microwave resonance approach, and suggests that the resonator behaves in a predictable way, consistent with known properties of OFHC copper, over the entire temperature range of interest. This opens the door to the application of other literature properties of copper (such as the isothermal compressibility κ_T) in future measurements and forms an important step toward the development of low-temperature refractive index gas thermometry at NRC.

Acknowledgements The authors would like to thank the National Institute of Standards and Technology (NIST) for the loan of the copper resonator used in this study; Robin Underwood and Eric May for sharing their computer codes for network analyzer interfacing and LM fitting; and Mike Moldover, Jim Mehl and Jim Schmidt for useful discussions.

References

1. H. Preston-Thomas, Metrologia **27**, 3 (1990). doi:10.1088/0026-1394/27/1/002
2. H. Preston-Thomas, Metrologia **27**, 107 (1990). doi:10.1088/0026-1394/27/2/010
3. J. Fischer, M. de Podesta, K.D. Hill, M. Moldover, L. Pitre, R. Rusby, P. Steur, O. Tamura, R. White, L. Wolber, Int. J. Thermophys. **32**, 12 (2011). doi:10.1007/s10765-011-0922-1
4. C. Gaiser, B. Fellmuth, N. Haft, Int. J. Thermophys. **31**, 1428 (2010). doi:10.1007/s10765-010-0802-0
5. L. Pitre, M.R. Moldover, W.L Tew, Metrologia **43**, 142 (2006). doi:10.1088/0026-1394/43/1/020
6. A.R. Colclough, Metrologia **10**, 73 (1974). doi:10.1088/0026-1394/10/2/006
7. R.L. Rusby, Inst. Phys. Conf. Ser. for Eur. Conf. on Temp. Meas. **26**, 44 (1975).
8. E.F. May, L. Pitre, J.B. Mehl, M.R. Moldover, J.W. Schmidt, Rev. Sci. Instrum. **75**, 3307 (2004). doi:10.1063/1.1791831
9. J.W. Schmidt, R.M. Gavioso, E.F. May, M.R. Moldover, Phys. Rev. Lett. **98**, 254504 (2007). doi: 10.1103/PhysRevLett.98.254504
10. J.B. Mehl, Metrologia **46**, 554 (2009). doi:10.1088/0026-1394/46/5/020
11. R.J. Underwood, J.B. Mehl, L. Pitre, G. Edwards, G. Sutton, M. de Podesta, Meas. Sci. Technol. **21**, 075103 (2010). doi:10.1088/0957-0233/21/7/075103
12. L. Pitre, F. Sparasci, D. Truong, A. Guillou, L. Risegari, M.E. Himbert, Int. J. Thermophys. **32**, 1825 (2011). doi:10.1007/s10765-011-1023-x
13. G. Edwards, R.J. Underwood, Metrologia **48**, 114 (2011). doi:10.1088/0026-1394/48/3/005
14. N.J Simon, E.S. Drexler, R.P. Reed, NIST Monograph **177** (1992).
15. J.G. Hust, A.B. Lankford, National Bureau of Standards Internal Report NBSIR **84**-3007 (1984).
16. B. Podobedov, Phys. Rev. ST Accel. Beams **12**, 044401 (2009). doi: 10.1103/PhysRevSTAB.12.044401

17. NIST Cryogenic Materials Properties Database, OFHC Copper (UNS C10100/C10200) entry, revised 02/03/2010, *http://cryogenics.nist.gov/MPropsMAY/OFHC%20Copper/OFHC_Copper_rev1.htm* (2010).